AIAA/AAS Astrodynamics Specialist Conference and Exhibit
21 - 24 August 2006, Keystone, Colorado

AIAA 2006-6660

Landmark Navigation Studies and Target Characterization in the Hayabusa Encounter with Itokawa

R. Gaskell[1], O. Barnouin-Jha[2], D. Scheeres[3], T. Mukai[4], N. Hirata[7],
S. Abe[4], J. Saito[5], M. Ishiguro[5], T. Kubota[5], T. Hashimoto[5], J. Kawaguchi[5],
M. Yoshikawa[5], K. Shirakawa[6], T. Kominato[6]. [1]JPL/Caltech, [2]APL/JHU, [3]U. Michigan,
[4]Kobe University, [5]JAXA/ISAS, [6]NEC Aerospace Systems, [7]U. Aizu.

1. Introduction

On 12 September 2005, the Japanese Hayabusa spacecraft arrived at the asteroid 25143 Itokawa. Due to Itokawa's small size (~550 meters) and low gravity, the spacecraft did not orbit, but hovered near each of two stations on a line between the asteroid and Earth. It remained at the "Gate Position" at a range of about 18 km until September 30, and then shifted to the "Home Position" at a range of about 7 km. Between October 8 and 28, it made several excursions to higher phase locations to obtain varying illumination conditions, and away from the equator to obtain polar data. On November 4, 9 and 12, the spacecraft made approaches to the asteroid in preparation for touchdowns on November 20 and 26.

Among the instruments carried on board the spacecraft (Fujiwara, et, al, 2006) were a narrow angle (AMICA) science camera (Nakamura, et al, 2001), a laser altimeter (LIDAR), and two wide-angle navigation (NAV) cameras, one co-aligned with AMICA, and one offset by about 45 degrees. During the station-keeping phase, navigation was accomplished by locating the center of brightness in the co-aligned NAV camera to establish the cross line of sight location, and using the LIDAR to establish the range. Errors occurred due to uncertainties in camera pointing and in the asteroid shape model.

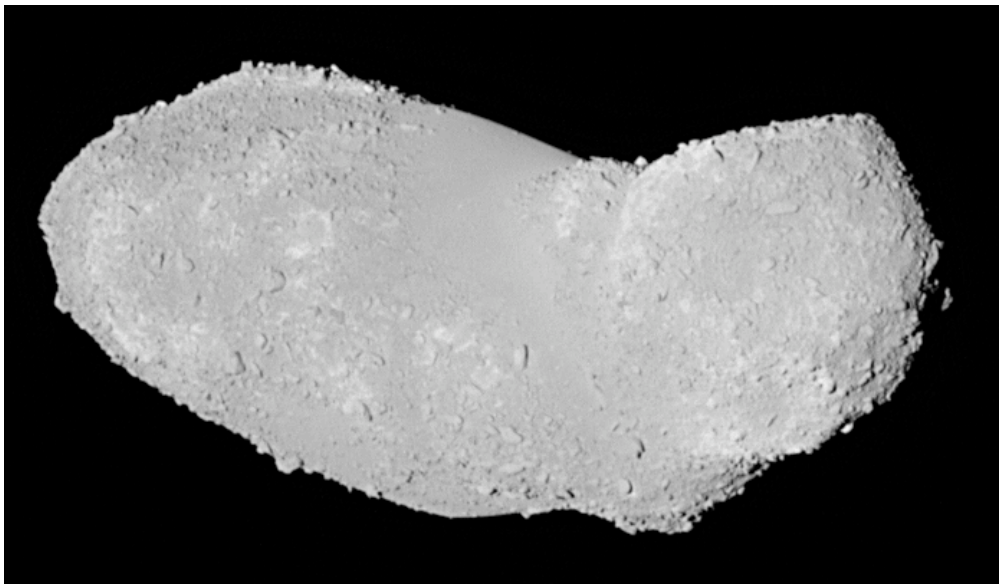

Figure 1. AMICA image 2423264117 of Itokawa.

Figure 1 shows a typical narrow-angle frame. Itokawa is in its "sea otter" orientation, with north toward the bottom of the image. About 770 of the more than 1500 AMICA images (Saito, et al, 2006) were used in this study, ranging in resolution from less than 10 cm/pixel to about 2 m/pixel. The earlier images were downloaded with lossless compression, but later ones were compressed with a JPEG algorithm that did not appreciably affect the data quality.

The basic data product of this analysis is an ensemble of digital topographic and relative albedo landmark maps (L-maps) constructed from imaging data using multiple-image stereography and photoclinometry. The stereo pair in Figure 2 clearly shows both the topography and albedo variations within such a map. Because of their three-dimensional structure, landmark maps can be aligned with images, limbs and other maps to find landmark location, spacecraft position and orientation, and the rotational properties of the target. They can also be combined to construct high-resolution topographic maps of portions of the surface or a global topography model (GTM) accurately depicting both the shape and topography of the body.

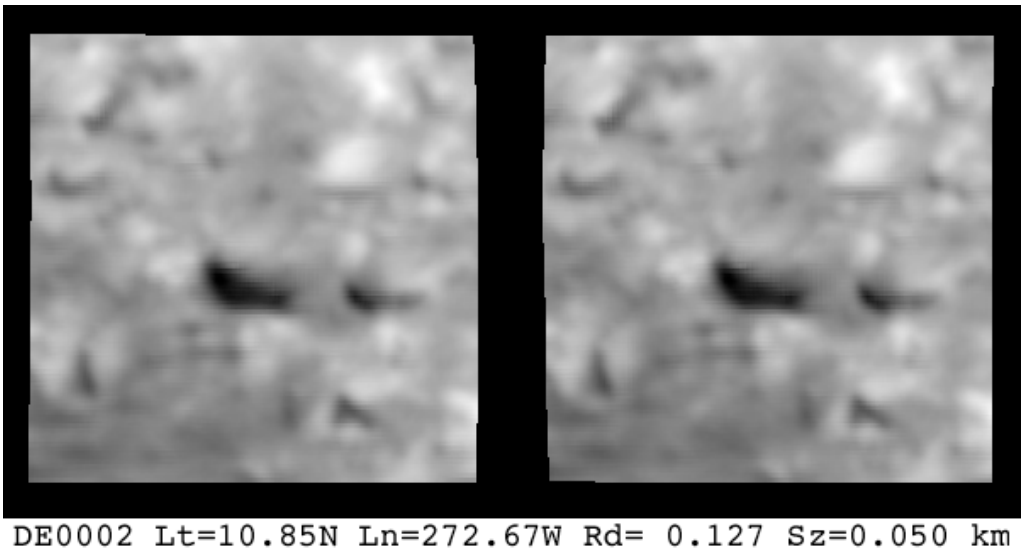

Figure 2. Landmark map (L-Map) DE0002 in stereo

In section 2, we discuss the methods used in this analysis. Sections 3 and 4 present surface characterization and navigation results respectively. Section 5 discusses work remaining to be done.

2. Methodology

1. L-map to image connection

At the heart of the analysis is the connection between the location of a pixel on an L-map and its predicted location in an image. This connection depends upon the location, orientation and height variation of the L-map, the location and orientation of the camera (spacecraft), and the rotational dynamics of the body. A change in any of these

quantities results in a characteristic change in the image-space projections, leading to their estimation in terms of the imaging data.

An L-map is specified by a vector **V** from the center of a body fixed coordinate system to the origin of the L-map coordinate system, by the axes of that coordinate system $\mathbf{u}_i$ (i=1,3), and by heights and albedos at positions (x,y) relative to that system. The L-map coordinates of a body-fixed point **P** on the surface are $x=\mathbf{u}_1\bullet(\mathbf{P}-\mathbf{V})$ and $y=\mathbf{u}_2\bullet(\mathbf{P}-\mathbf{V})$ with the height $h(x,y)=\mathbf{u}_3\bullet(\mathbf{P}-\mathbf{V})$ and an albedo a(x,y). The camera's position vector **W** and its coordinate system $\mathbf{c}_i$ (i=1,3), unit vectors in the sample, line and boresight directions, respectively, are also specified in body-fixed coordinates.

For a simple narrow angle camera with focal length f, the focal plane image location X_i (i=1,2) of the L-map center **V** is given by

$$X_i = f(\mathbf{V}-\mathbf{W})\bullet\mathbf{c}_i/(\mathbf{V}-\mathbf{W})\bullet\mathbf{c}_3 \qquad (1)$$

If $M_{ij}=\mathbf{c}_i\bullet\mathbf{u}_j$, a point (x,y,h) on the L-map has the focal plane projection then

$$X_i = f((\mathbf{V}-\mathbf{W})\bullet\mathbf{c}_i+M_{i1}x+M_{i2}y+M_{i3}h)/((\mathbf{V}-\mathbf{W})\bullet\mathbf{c}_3+M_{31}x+M_{32}y+M_{33}h) \qquad (2)$$

An equally important connection is between the slopes and albedos within an L-map, the local illumination and camera directions, and the predicted image-space brightness. A change in slope or albedo at any L-map pixel will result in a characteristic change in the predicted brightness at the corresponding location in an image. At the point (x,y) of the L-map, the brightness at the corresponding focal plane location in the kth image can be parameterized as

$$I_k(x,y,\mathbf{t}) = \Lambda_k(1+t_3(x,y))F(\cos i,\cos e) + \Phi_k \qquad (3)$$

F is an appropriate reflectance function (Hapke,1981; Squyres and Veverka, 1982). The factor $(1+t_3)$ is the relative albedo at map coordinates (x,y), normalized so that $\langle t_3\rangle=0$ over the map, and *i* and *e* are the local angles of incidence and emission, relative to the surface normal at (x,y). During its extraction, the imaging data is usually scaled (maximally stretched), so the multiplier Λ_k is included. Moreover, due to background or haze in some images, or perhaps because super-resolution sampling has left a "washed out" look, a positive background term Φ_k can be added.

In terms of the (negative) slopes $t_1=-dh/dx$ and $t_2=-dh/dy$, the local arguments of the function F are

$$\cos i = (s_1t_1+s_2t_2+s_3)/\sqrt{(1+t_1^2+t_2^2)} \qquad (4a)$$

$$\cos e = (e_1t_1+e_2t_2+e_3)/\sqrt{(1+t_1^2+t_2^2)} \qquad (4b)$$

where $s_j=\mathbf{s}\bullet\mathbf{u}_j$ and $e_j=\mathbf{e}\bullet\mathbf{u}_j$ are the L-map components of the sun and spacecraft unit vectors respectively. The reflectance function

$$F(\cos i, \cos e) = \cos i + 2\cos i/(\cos i + \cos e) \quad (5)$$

is used, since it does a good job rendering high resolution shape models. No phase dependence has been included since it is nearly constant over each L-map, even for wide-angle images, and any phase functions can be absorbed into Λ_k .

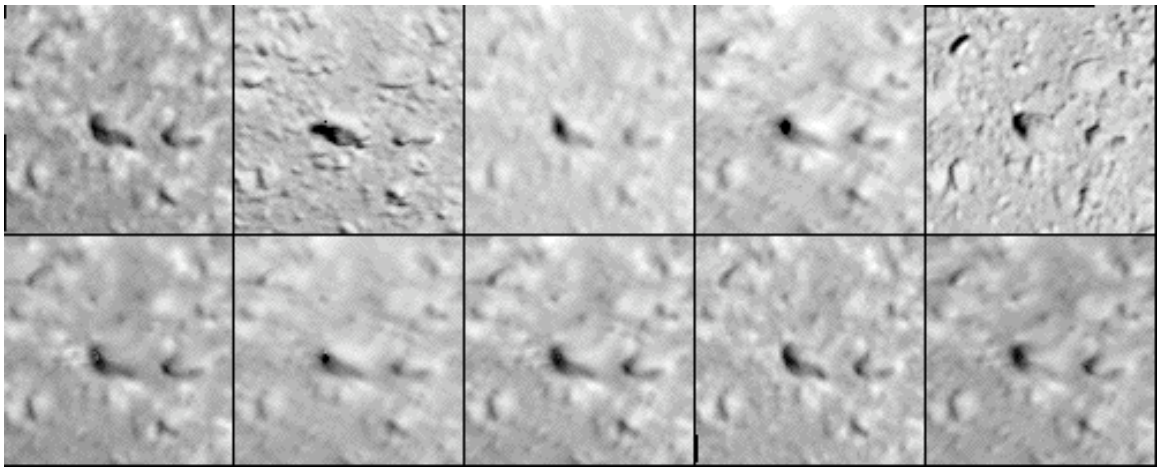

Figure 3. Imaging data and re-illuminated L-map DE0002.

The top row of Fig. 3 displays data extracted from five AMICA images, projected onto the coordinates of the L-map displayed in Fig. 2 according to equation 2). The bottom row shows the corresponding L-map illuminated according to equation 3), with the Λ_k adjusted to match the average brightness in the overlapping regions.

In addition to its appearance on the image of a body, the three-dimensional structure of an L-map allows it to be identified on the limb. The focal plane location of the map center, which is not necessarily on the limb, is still determined by equation 2). The predicted limb points are those parts of the L-map surface to which the line of sight is tangent, and which are not either hiding or hidden by any other part of the body.

A final constraint on the L-map lies not with its correlation with imaging data, but with other L-maps. The common topography of the overlapping maps can be aligned in three-dimensions to solve for the central vector **V** of one L-map relative to the other.

2. Geometry estimation

The geometry problem consists of determining the body fixed L-map vectors **V**, the body's pole, and the spacecraft location **W** and orientation **c**. The L-map topography problem is treated as a separate estimation. The geometry solution is found by minimizing the quantity

$$H = \Sigma K(Y_i - X_i)^2 + H_E \quad (6)$$

with respect to variations in **V**, **W**, **c**, or rotational parameters **g**. Y_i (i=1,2) are the measured focal plane locations of the L-map centers and where the predicted locations X_i (i=1,2) come from equation 1). The sum is over all L-maps and all images, with each term weighted by a different "spring constant" K, the inverse square measurement uncertainty. The H_E represent external *a priori* terms which constrain the estimation according to external measurements. The solution proceeds iteratively, solving in turn for all the L-map vectors **V**, and then for the spacecraft positions and orientations **W** and **c**. Formal uncertainties from each solution help determine the weights K of the next.

The solution for an L-map vector $\mathbf{V} + \delta\mathbf{V}$ is found by minimizing

$$H = \Sigma K(Y_i - X_i - \delta\mathbf{V} \bullet \nabla_V X_i)^2 + \Sigma K_m (\mathbf{V}_m + \Delta_m - \mathbf{V} - \delta\mathbf{V})^2 \qquad (7)$$

where X_i is evaluated at the nominal vector **V**, and $\nabla_V X_i$ are the partials of X_i with respect to the components of **V**. The first sum is over all images containing the landmark, while the second, coming from H_E, is over all overlapping L-maps. Δ_m is the difference between the two central L-map vectors from the correlation discussed at the end of Section 1. The minimum of H in equation 7) occurs when

$$\Sigma K \nabla_V X_i (Y_i - X_i - \nabla_V X_i \bullet \delta\mathbf{V}) + \Sigma K_m (\mathbf{V}_m + \Delta_m - \mathbf{V} - \delta\mathbf{V}) = 0 \qquad (8)$$

which can be written as

$$\mathbf{M} \bullet \delta\mathbf{V} = \mathbf{r} \qquad (9)$$

with $\mathbf{M} = \Sigma K \nabla_V X_i \otimes \nabla_V X_i + \Sigma K_m \mathbf{I}$ and $\mathbf{r} = \Sigma K \nabla_V X_i (Y_i - X_i) + \Sigma K_m (\mathbf{V}_m + \Delta_m - \mathbf{V})$. The 3x3 matrix **M** is inverted to solve equation 9) for the corrections $\delta\mathbf{V} = \mathbf{M}^{-1} \bullet \mathbf{r}$. The diagonal elements of $\mathbf{M}^{-1}$ are the squares of the formal uncertainties in **V**.

The solutions for spacecraft position $\mathbf{W} + \delta\mathbf{W}$ and orientation $\mathbf{c}_i + \varepsilon_{ijk}\mathbf{c}_j\delta\alpha_k$ are found by minimizing

$$\begin{aligned} H = {} & \Sigma K(Y_i - X_i - \delta\mathbf{W} \bullet \nabla_W X_i - \delta\boldsymbol{\alpha} \bullet \nabla_\alpha X_i)^2 + K_n(\mathbf{W}_n - \mathbf{W} - \delta\mathbf{W})^2 \\ & + K_n(\varepsilon_{ijk}\, \mathbf{c}_{ni} \bullet \mathbf{c}_j - \delta\alpha_k)^2 + \Sigma K_p(\mathbf{W}_p + \Delta_p - \mathbf{W} - \delta\mathbf{W})^2 \end{aligned} \qquad (10)$$

The sum in the first term is over all landmarks occurring in the image, with the K determined from the formal uncertainties of the previous estimation. The second two terms reflect nominal positions, orientations and, through the K_n, the corresponding uncertainties. These come, for example, from external radiometric, optical navigation and star-tracker measurements. The final term is a sum over those images correlated with the image in question, those that are close enough in time so that the position difference Δ_p can be predicted by the trajectory dynamics. This term ties images together in the same way that the last term in equation 7) ties L-maps together. The minimization of H in equation 10) results in a set of six equations for the six corrections $\delta\mathbf{W}$ and $\delta\boldsymbol{\alpha}$.

A change in the rotation of the body alters the components of the vectors in the body-fixed frame in a time-dependent fashion. It does not affect the scalars $\mathbf{W}\bullet\mathbf{c}$ in equation 1) since both vectors are associated with a single image and are transformed in the same way. The products $\mathbf{V}\bullet\mathbf{c}$ will change, however, both because the components of $\mathbf{V}$ and the $\mathbf{c}$ change, and because the new geometry yields a new solution for the L-map vectors. The corrections to the rotational parameters $\mathbf{g}$ and the L-map vectors $\mathbf{V}$ are determined by minimizing

$$H = \Sigma K(Y_i - X_i - \delta\mathbf{g}\bullet\nabla_g X_i - \delta\mathbf{V}\bullet\nabla_V X_i)^2 \qquad (11)$$

summed over all images and all landmarks. The resulting equations are

$$\mathbf{A}\bullet\delta\mathbf{g} + \Sigma\, \mathbf{C}_k^{\mathrm{T}}\bullet\delta\mathbf{V}_k = \mathbf{r}_0 \qquad \text{and} \qquad \mathbf{C}_k\bullet\delta\mathbf{g} + \mathbf{B}_k\bullet\delta\mathbf{V}_k = \mathbf{r}_k \qquad (12)$$

where k labels the L-maps and

$$\begin{aligned}
&\mathbf{A} = \Sigma K\nabla_g X_i \otimes \nabla_g X_i && \text{(sum over all images and L-maps)}\\
&\mathbf{B}_k = \Sigma K\nabla_{Vk} X_i \otimes \nabla_{Vk} X_i && \text{(sum over all images with L-map k)}\\
&\mathbf{C}_k = \Sigma K\nabla_{Vk} X_i \otimes \nabla_g X_i && \text{(sum over all images with L-map k)}\\
&\mathbf{r}_0 = \Sigma K(Y_i - X_i)\nabla_g X_i && \text{(sum over all images and L-maps)}\\
&\mathbf{r}_k = \Sigma K(Y_i - X_i)\nabla_{Vk} X_i && \text{(sum over all images with L-map k)}
\end{aligned} \qquad (13)$$

In practice, the $\delta\mathbf{V}$ are eliminated from equations 12) to give

$$(\mathbf{A} - \Sigma\, \mathbf{C}_k^{\mathrm{T}}\mathbf{B}_k^{-1}\mathbf{C}_k)\bullet\delta\mathbf{g} = \mathbf{r}_0 - \Sigma\, \mathbf{C}_k^{\mathrm{T}}\mathbf{B}_k^{-1}\mathbf{r}_k \qquad (14)$$

which is solved for the rotational correction $\delta\mathbf{g}$. The spacecraft positions $\mathbf{W}$ and orientations $\mathbf{c}$ are then expressed in the new body-fixed frame and equation 9) is used to find the new L-map vectors $\mathbf{V}$.

3. Topography estimation

Each L-map is typically about a hundred pixels square. At each of these pixels (x,y), the values of t_i are solved for by fitting the extracted brightness data $E_k(x,y)$ to equation 3) and minimizing the weighted sum squared residual

$$H = \Sigma K\,(E_k(x,y) - I_k(x,y,\mathbf{t}) - \delta\mathbf{t}\bullet\nabla_t I_k(x,y,t))^2 \qquad (15)$$

where the sum is over the images. Λ and Φ are determined from a global fit over the L-map at the nominal values of $\mathbf{t}$.

The minimization of H is accomplished by setting its partials with respect to $\delta\mathbf{t}$ equal to zero. This yields a set of three coupled linear equations of the form $\mathbf{M}\delta\mathbf{t} = \mathbf{w}$, where the information matrix $\mathbf{M}$ is quadratic in the partials of I, and $\mathbf{w}$ is made up of products of the partials and the residuals. The inverse of the information matrix, $\mathbf{M}^{-1}$, is

the covariance matrix. Its diagonal elements measure the formal uncertainties σ^2 in the corresponding variables. To **M** is added a diagonal *a priori* information matrix **D** to keep the solution from diverging. In particular, if the albedo component D_{33} is large, albedo variations will be tightly constrained. This is often done initially, to allow time for the topography solution to settle down.

Notice that the slopes determined in this way do not implicitly satisfy the "curl-free" condition $\partial_1 t_2 - \partial_2 t_1 = 0$, which follows from $\partial_1 \partial_2 h - \partial_2 \partial_1 h = 0$. However, the nominal values of t_1 and t_2 used in the estimation are found from the height solutions described below and are manifestly curl-free, so as the iteration proceeds, the condition is eventually satisfied.

The height at each location (x,y) is determined from the neighboring heights, and a possible constraining height h_c from the shape model, differential stereography, limb or overlapping map data, according to:

$$\begin{aligned} h(x,y) = [&h(x+s,y)+s(t_1(x,y)+t_1(x+s,y))/2+h(x-s,y)-s(t_1(x,y)+t_1(x-s,y))/2 \\ &+h(x,y+s)+s(t_2(x,y)+t_2(x,y+s))/2+h(x,y-s)-s(t_2(x,y)+t_2(x,y-s))/2 \\ &+w_c h_c(x,y)+]/(w_c+4), \end{aligned} \tag{16}$$

where s is the map pixel spacing and w_c is a small constraining weight. This equation is applied repeatedly to map points chosen at random until a converged solution is reached. If any height does not exist, its term is not included in the average.

3. Surface Characterization

About 300 L-maps were constructed during the encounter itself, and were gradually refined as more images were added and as the navigation solution converged. The entire process was an iterative one, involving solutions for L-map topography and albedo, body fixed L-map centers, spacecraft location and orientation, and the asteroid's shape and rotational axis. The nominal shape and pole were provided by radar observations (Ostro, et al, 2004). Since data for the polar regions did not become available until the end of October, global map coverage was not achieved until early November. Since then about 500 higher resolution maps have been added.

The ensemble of L-maps can be used to produce a local topography map by averaging the L-map heights and slopes relative to a flat reference surface. The averaged slopes are then integrated as in Eqn. 16 to produce the height distribution, with a sparse set of averaged heights h_c conditioning the process. Figure 4 is a stereo pair of such a map, showing the Yoshinodai boulder. In this process, only topography is included. The albedo information has been discarded. The local topography maps can also be used to re-sample an image in order to display the finer topography and the albedo variations. Figure 5 shows such a re-sampling of the region surrounding the Pencil boulder. Both of maps are about 100 meters square.

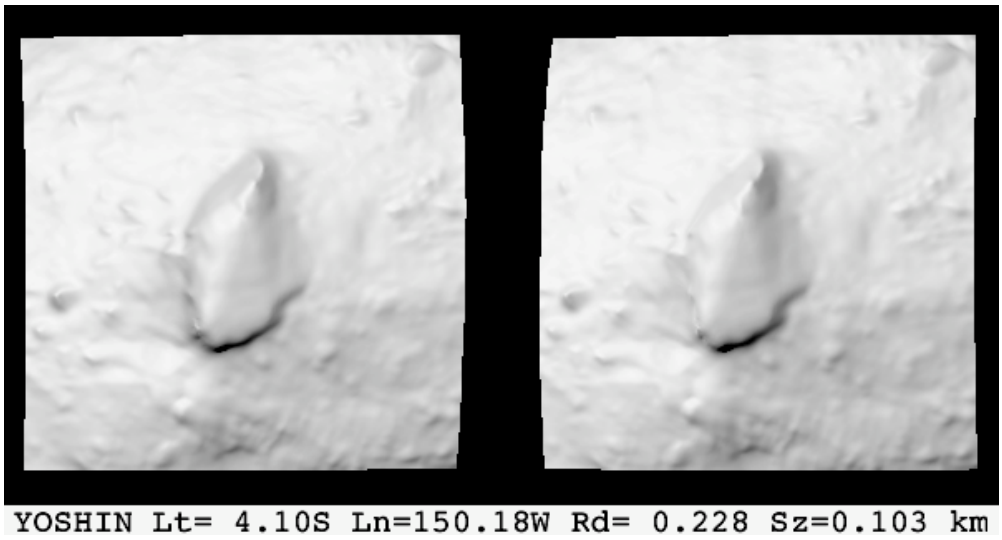

Figure 4. Stereo pair of the Yoshinodai boulder.

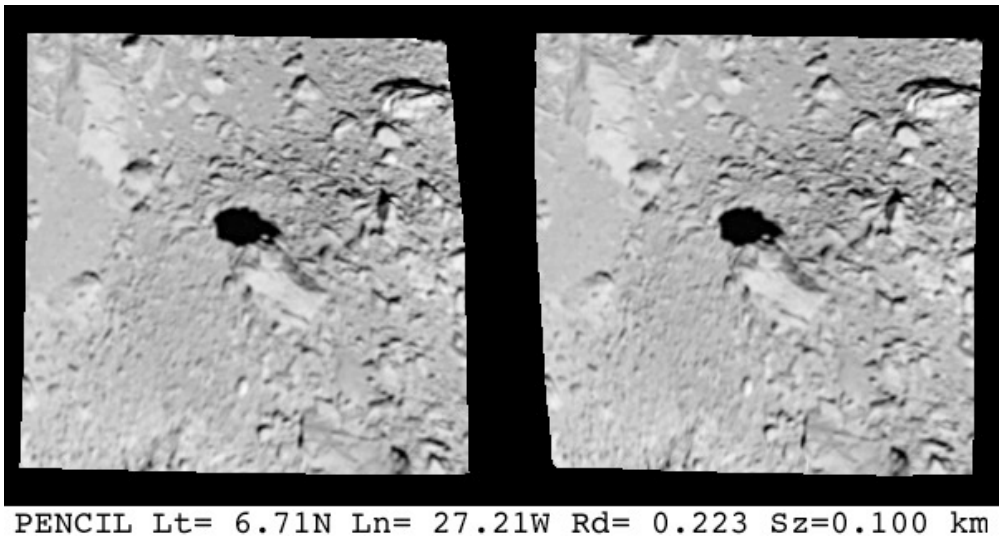

Figure 5. Resampled stereo pair of the Pencil boulder.

The global topography model (GTM) is constructed by a similar procedure, but referred to a pre-existing approximate shape model rather than a plane. In practice, a chain of models is produced, having 6000, 25000, 100000, 400000 and 1.6 million vectors respectively, with each acting as the reference shape for the next. Figure 6 shows the GTM illuminated as in Fig. 1, and with the L-map of Figs. 2 and 3 displayed. Notice that the map is upside down since north is at the bottom of the picture.

The surface area is 0.404 km^2 and the volume is .0177 km^3, with uncertainties of less than one percent. The principal moments per unit mass are (.00631, .02127, .02236) km^2. The pole, determined from a simultaneous estimation with landmark locations, is 90.02°, -67.03° (earth equatorial) or 269.03°, -89.53° (ecliptic), with an uncertainty of 0.005°.

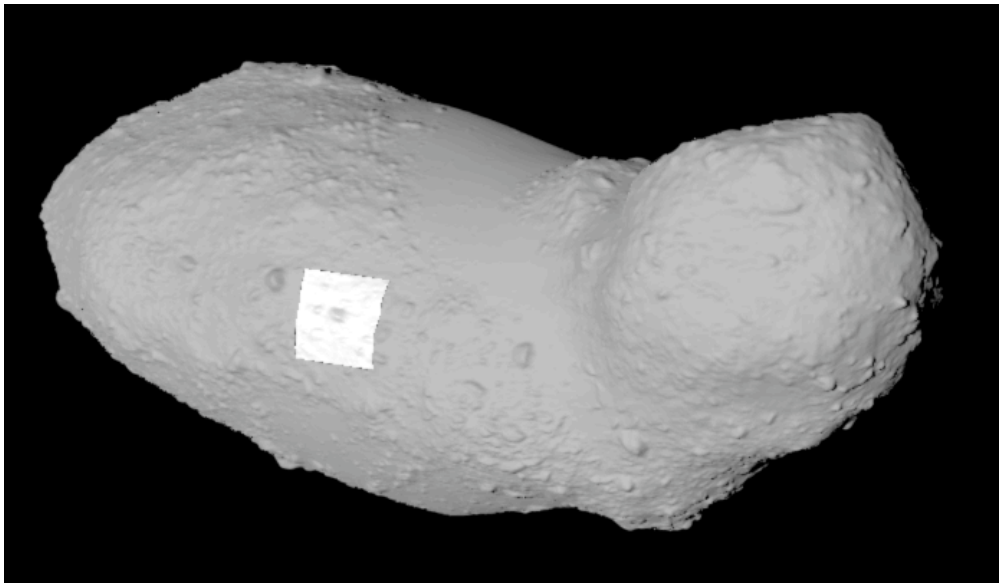

Figure 6. Global topography model and L-map DE0002.

3. Navigation

The navigation function of the analysis software was crucial to the success of this work because spacecraft position information provided in the SPK files was often unreliable. For example, one early image was reported at a range of 6.73 km. Initial registration corrected this to 20.59 km and alignment with L-maps gave the value 20.45 km. After LIDAR and dynamic corrections, the final value of 20.39 km was obtained.

The 60-meter difference between the L-map only and the L-map with LIDAR values is typical, and reflects the uncertainties inherent in the estimation of Eqn. 10 in the absence of the final dynamical term. Essentially, the problem lies in finding the overall scale of the solution. For orbital missions, this scale is provided by Doppler data since the absolute distance between two observations can be determined by integrating the velocity. For a hovering mission, the LIDAR provides this scale. Note that the LIDAR provides the range to the surface, so the actual range to the center depends on the GTM. The 60 m range error without LIDAR corresponds to a 0.3% error in scale, or a 50 cm error in the over all size of Itokawa. The next iteration has rms range residuals of about 4 meters, with size errors far below the 20-centimeter rms residuals of the L-map estimation

For a narrow angle camera, it is difficult to distinguish between clock/cone pointing errors and cross line-of-sight spacecraft position errors. Fortunately, the Hayabusa pointing information was good, its one mrad uncertainty translating into a 20 m uncertainty at the 20 km gate position, and a 7 m uncertainty at the 7 km home position. By fitting freefall trajectories to the positions determined by L-maps and LIDAR, and for intervals between maneuvers, the random errors could be reduced. The resulting image-to-image correlations were included in the final term of Equation. 10 to condition the

solutions. The final uncertainties in position were about 1.5 meters at the home position and 4 meters overall. The position solution for the 773 AMICA images used so far is shown in Fig. 7. The coordinate system is a pseudo-inertial one with the z-axis pointing from Itokawa to the Earth, and the sun direction in the x-z plane.

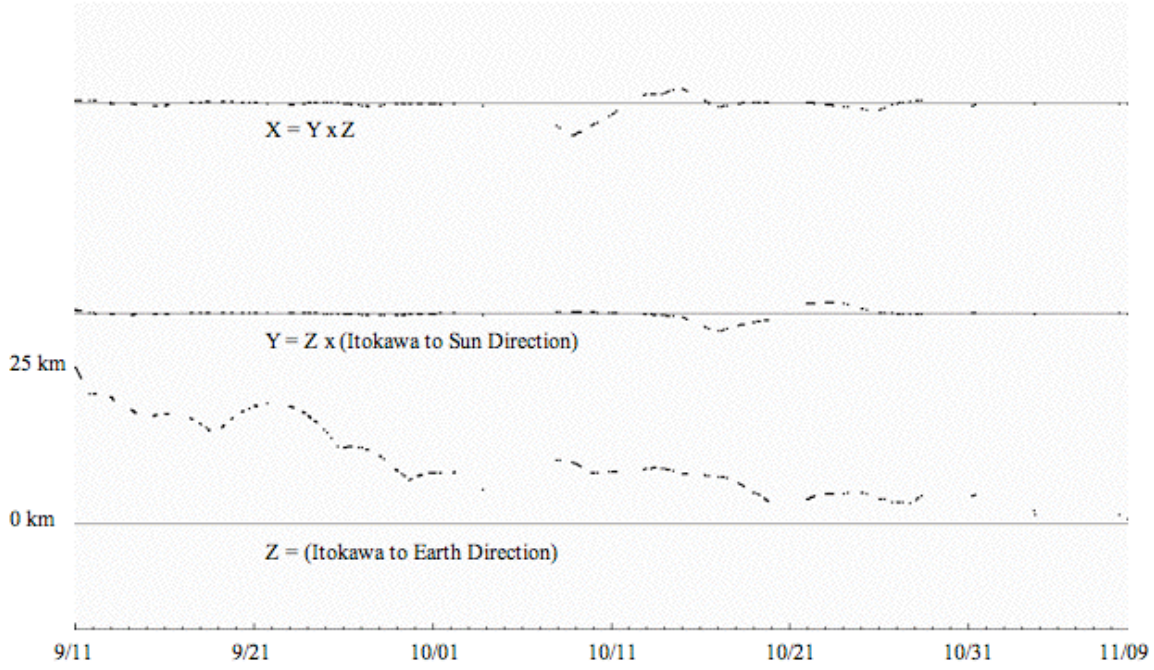

Figure 7. Spacecraft positions for 773 AMICA images.

One application envisioned for the L-map technology is its use in semi-autonomous navigation during approach and landing (Gaskell, 2001). L-maps constructed on the ground during the observation phase from narrow-angle camera data can be correlated on board with wide-angle image data to rapidly determine spacecraft location and orientation. Twelve of the wide-angle frames downloaded during the November 12 approach with slant ranges varying from 57 m to 740 m were correlated with L-maps. The rms difference between the predicted ranges and the measured LIDAR ranges was about 10 meters. The final two images in the sequence had the largest errors, possibly because the LIDAR was moving off the body. When these were removed, the rms residual dropped to 4 meters. A display from the L-map correlation of one of these images is shown in Figure 8, with alternate rows showing extracted imaging data and corresponding L-map data. Note the spacecraft's shadow in the first two boxes. The shadow appeared in ten of the images, and was used to determine the precise camera pointing. Despite the difference in resolution, and the very lossy compression of the wide-angle data, the software was able to perform the correlations.

The body-fixed positions determined from this analysis are plotted in Figure 9. A trajectory fit to the data was used to solve for the mass of Itokawa with the result GM = $2.36 \times 10^{-9} \pm 0.15 \times 10^{-9}$ km^3/s^2. With the .0177 km^3 volume from the GTM, the density becomes .02.0 g/cm^3 of suggesting a porous interior.

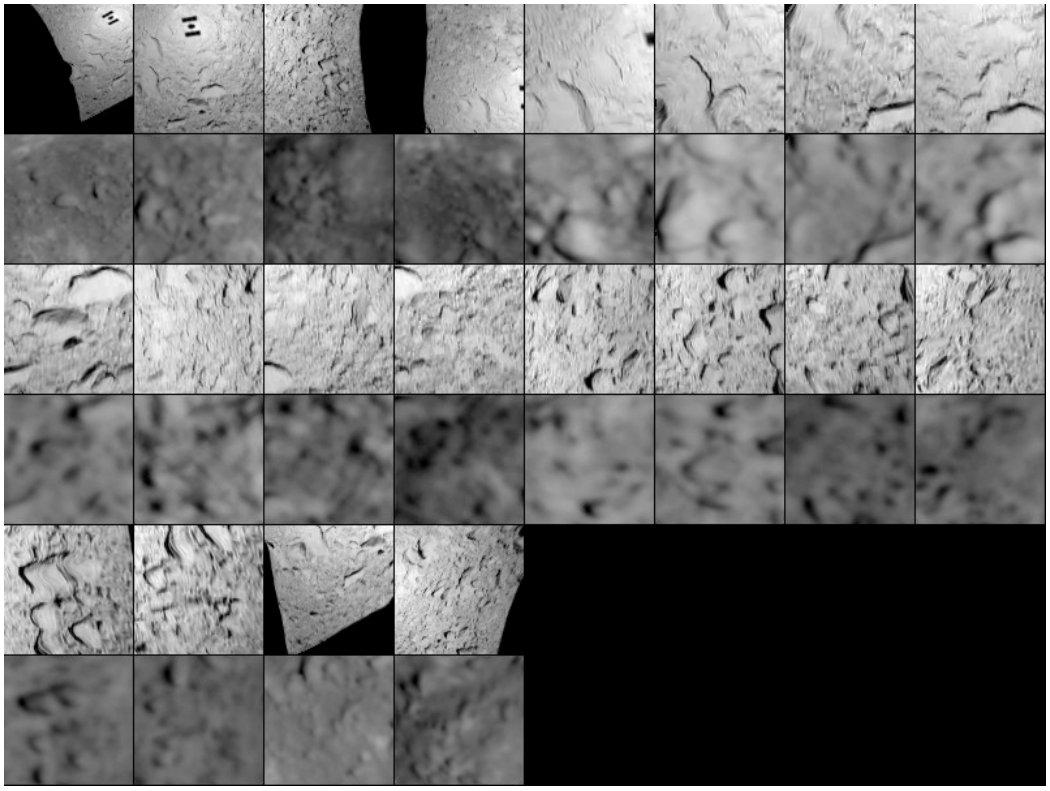

Figure 8. Auto-registration of a wide-angle navigation frame.

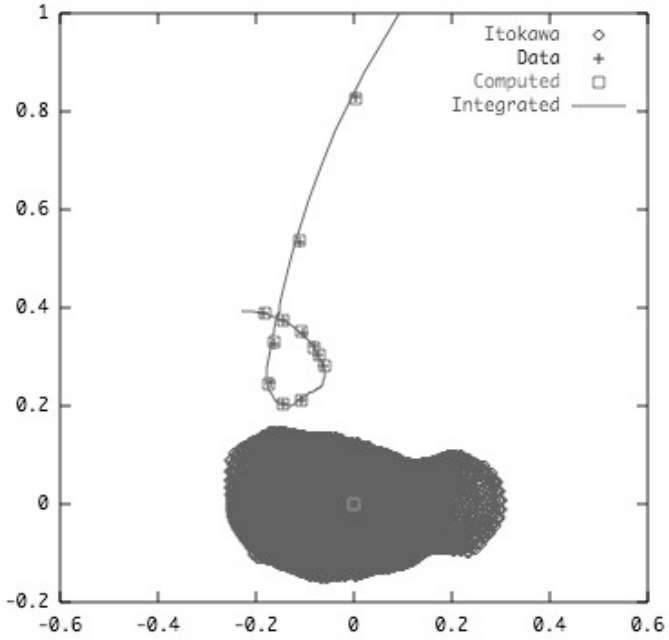

Figure 9. Body-fixed trajectory of Nov. 12 approach.

5. Discussion

Our analysis software proved very successful in characterizing the shape and topography of Itokawa and in determining the spacecraft trajectory. Almost as successful was the simulation that preceded the encounter. The current L-map residuals are 16 cm, compared with the simulation value of 21 cm. Our pole uncertainty of .005° was identical to the simulation's error. Finally, the simulation error of 2.4 m at the 7 km home position was larger than our estimate of 1.5 m, but the simulation did not directly include the LIDAR data type.

There is still work to do in the analysis, including creation of another level of higher resolution L-maps, the creation of a global albedo map, the inclusion of maneuvers in the trajectory analysis, and the archiving of the L-map and navigation data.

References

A. Fujiwara, et al. (2006), "The Rubble-Pile Asteroid Itokawa as Observed by Hayabusa," Science 312, 1330-1334.

R. Gaskell, et al. (2006), "Global Topography of Asteroid 25143 Itokawa," 37th LPSC, Houston.

R. Gaskell (2005), "Landmark Navigation and Surface Characterization in a Simulated Itokawa Encounter," AAS paper 05-289, AAS/AIAA Astrodynamics Specialists Conf., Lake Tahoe.

R.W. Gaskell (2001), "Automated Landmark Identification for Spacecraft Navigation," AAS paper 01-422, AAS/AIAA Astrodynamics Specialists Conf., Quebec.

B. Hapke (1981), "Bidirectional Reflectance Spectroscopy, I. Theory," Journal of Geophysical Research 86, 3039-3054.

T. Nakamura, et al (2001), "Multi-band imaging camera and its sciences for the Japanese Near-Earth Asteroid Mission MUSES-C," Earth Planets Space 53, 1047-1063.

S. Ostro. et al. (2004), "Radar Observations of Asteroid 25143 Itokawa (1998SF36)," Meteoritics and Planetary Science 39(3), 407-424.

J. Saito *et al*. (2006), "Detailed Images of Asteroid 25143 Itokawa from Hayabusa," Science 312, 1341-1344.

T. Nakamura, et al (2001), "Multi-band imaging camera and its sciences for the Japanese Near-Earth Asteroid Mission MUSES-C," Earth Planets Space 53, 1047-1063.

.S. Squyres and J. Veverka (1982), "Variation of Albedo with Solar-Incidence Angle on Planetary Surfaces," Icarus 50, 115-122.